Multi-epoch combination of direct imaging observations for exoplanet detection

Jules Dallant, Maud Langlois, Eric Thiébaut, Olivier Flasseur

AO4ELT7 - June 2023 - Avignon

Multi-epoch combination of direct imaging observations for exoplanet detection

Jules Dallant, Maud Langlois, Éric Thiébaut, and Olivier Flasseur

CRAL, CNRS, Université de Lyon, ENS, Saint-Genis-Laval, France

ABSTRACT

Detecting exoplanets by direct imaging is a difficult task that systematically requires the use of advanced post-processing algorithms in addition to an efficient adaptive optics and coronagraphic system. The upcoming thirty meters class telescopes will enable exploring the inner stellar environments where the typical contrast levels to reach will require long exposure times only achievable by combining several observations conducted days, weeks, or months apart. For such observations, the orbital motion of exoplanets will no longer be negligible, and a proper orbital modeling will be crucial to combine multi-epoch observations without drastically degrading the detection confidence and the achievable contrast. In that context, we recently developed the PACOME algorithm which efficiently combines observations of the same star while accounting for the Keplerian motion of the sought exoplanets within an end-to-end statistical detection formalism. The sensitivity and reliability of the proposed method constitute major advantages in the field to detect new companions at a statistically grounded confidence level. In this paper, we consider a case-study example of thirteen VLT/SPHERE-IRDIS observations of the HD 95086 system, and we illustrate the efficiency of the PACOME by (re-)detecting HD 95086 b with a very high multi-epoch signal-to-noise ratio of 53.7. We also derive its orbital elements posterior distributions.

Keywords: Instrumentation: high angular resolution, techniques: image processing, methods: statistical, methods: data analysis, planets and satellites: detection, stars: HD 95086.

1. INTRODUCTION

Direct imaging exoplanet detection and characterization require combining extreme adaptive optics with custom differential imaging techniques and dedicated post-processing algorithms to eliminate or account for the residual stellar leakages. Over the last decade, large efforts have been invested on new powerful post-processing algorithm (see [20, 3] for reviews). They currently allow the detection of massive exoplanets down to 10 au but their performance remain limited at shorter angular separations. One of the limiting factor, from a data processing point of view, is related to the lack of diversity induced by the processing of each epoch of observations individually. The upcoming thirty meters class telescopes such as the ELT, will enable exploring much deeper the inner environment of nearby solar-type stars. The contrast levels to reach will require long exposure times of several tens of hours, that will only be achieved by combining several observations conducted days, weeks, or months apart.

Send correspondence to: jules.dallant@univ-lyon1.fr

At these timescales and separations, the orbital motion of exoplanets will no longer be negligible, and a proper orbital modeling will be crucial to combine multi-epoch observations without drastically degrading the detection confidence and the achievable contrast. Very recently, we proposed the PACOME algorithm [5] that combines optimally several observations of the same star within an end-to-end matched filter based statistical detection formalism. It accounts for the Keplerian orbital motion of the sought exoplanets across epochs and co-adds constructively their weak signals. Its sensitivity and the reliability of its astrophysical outputs (orbital elements and their uncertainties) constitute major advantages in the field to detect new companions at a statistically grounded confidence level. Besides, its implementation is efficient and fully automatized, allowing to test and refine a large number of orbits in a reasonable computation time.

We present the mathematical framework of our method and derive its statistical guarantees in Sect. 2, apply and test its performances on a multi-epoch dataset of 13 observations of HD 95086 acquired with the SPHERE-IRDIS instrument, operating on the VLT, in Sect. 3 and draw the conclusions of this work in Sect. 4.

2. MULTI-EPOCH COMBINATION FORMALISM

2.1 Direct model

A typical angular and spectral differential imaging (ASDI) dataset consists of an hypercube of several 2-D frames per spectral channel. The PACO algorithm [11, 12] learns the statistical model of the nuisance of the data in small local patches of a few tens of pixels to remove the strong spatial correlations that lie within and to extract the signal of a potential source. Additionally, it reduces an hypercube down to a signal-to-noise ratio (S/N) map for each spectral channel. It is shown in [11, 13, 12] that, in the absence of source, the distribution of these S/N maps is well approximated by a normal law. However, since the stellar leakages are caused by the diffraction of the light in the presence of residual optical aberrations, the mono-epoch S/N maps of a given epoch t are spectrally correlated. Consequently, in order to combine properly the different S/N maps spectrally and temporally, and therefore to increase the detection sensitivity, the corresponding spectral correlations need to be learned and whitened beforehand.

We consider a multi-epoch datasets of T epochs. Each mono-epoch observation consist of K 2-D frames and L spectral channels. Let $\boldsymbol{x}_t \in \mathbb{R}^L$ be the collection of all temporo-spectral S/N at epoch t. Assuming a prior spectral spectrum can improve the detection of sources having a similar spectral energy distribution [12]*. Hence, at a given epoch t, we model $\boldsymbol{x}_t$ by:

$$\boldsymbol{x}_t = \alpha_t^{\text{int}}\, \boldsymbol{\gamma}_t \odot \boldsymbol{\beta}_t(\boldsymbol{\theta}_t(\boldsymbol{\mu})) + \boldsymbol{\epsilon}_t\,, \tag{1}$$

where $\odot$ denotes the pointwise product and where α_t^{int} is the spectrally integrated flux (0 in the absence of source), $\boldsymbol{\gamma}_t \in \mathbb{R}^L$ is the assumed spectrum of the point source (normalized between 0 and 1), $\boldsymbol{\beta}_t \in \mathbb{R}^L$ is a vector whose ℓ-th element is the inverse of the expected flux standard deviation of spectral channel ℓ, $\boldsymbol{\theta}_t(\boldsymbol{\mu}) \in \mathbb{R}^2$ is the 2-D projected position of the potential source along its orbit $\boldsymbol{\mu} \in \mathbb{R}^7$, and $\boldsymbol{\epsilon}_t \in \mathbb{R}^L$ is a random vector accounting for the fluctuations of the temporo-spectral S/N values that have a Gaussian distribution with zero mean and spectral covariance $\boldsymbol{\Sigma}_t$ such that:

$$\boldsymbol{\epsilon}_t \sim \mathcal{N}(\boldsymbol{0}, \boldsymbol{\Sigma}_t)\,. \tag{2}$$

2.2 Maximum likelihood estimation

Considering all epochs independent, the multi-epoch log-likelihood of the spectrally correlated data under the assumption of a prior spectrum $\boldsymbol{\gamma} = \{\boldsymbol{\gamma}_t\}_{t=1:T}$ writes:

$$\begin{aligned}
\mathscr{L}_{\boldsymbol{\gamma}}(\boldsymbol{\alpha}^{\text{int}}, \boldsymbol{\mu}) &= \sum_t \mathscr{L}_{t,\boldsymbol{\gamma}_t}(\alpha_t^{\text{int}}, \boldsymbol{\theta}_t(\boldsymbol{\mu})) \\
&= c_1 - \frac{1}{2}\sum_t \left\| \boldsymbol{x}_t - \alpha_t^{\text{int}} \boldsymbol{\gamma}_t\, \boldsymbol{\beta}_t(\boldsymbol{\theta}_t(\boldsymbol{\mu})) \right\|^2_{\boldsymbol{\Sigma}_t^{-1}} \\
&= c_2 + \sum_t \left[\alpha_t^{\text{int}} B_{t,\boldsymbol{\gamma}_t}(\boldsymbol{\theta}_t(\boldsymbol{\mu})) - \frac{1}{2}\left(\alpha_t^{\text{int}}\right)^2 A_{t,\boldsymbol{\gamma}_t}(\boldsymbol{\theta}_t(\boldsymbol{\mu})) \right]\,,
\end{aligned} \tag{3}$$

*This is a mild assumption. Even when the prior spectrum differs significantly from the truth, the contrast degradation remains modest [12].

where c_1 and c_3 are irrelevant constants, and where the $A_{t,\boldsymbol{\gamma}_t}$ and $B_{t,\boldsymbol{\gamma}_t}$ quantities are pre-calculated by PACO as described in [12]:

$$\begin{cases} A_{t,\boldsymbol{\gamma}_t}(\boldsymbol{\theta}) = \big(\boldsymbol{\gamma}_t\, \boldsymbol{\beta}_t(\boldsymbol{\theta})\big)^\mathsf{T}\, \boldsymbol{\Sigma}_t^{-1}\, \big(\boldsymbol{\gamma}_t\, \boldsymbol{\beta}_t(\boldsymbol{\theta})\big), \\ B_{t,\boldsymbol{\gamma}_t}(\boldsymbol{\theta}) = \big(\boldsymbol{\gamma}_t\, \boldsymbol{\beta}_t(\boldsymbol{\theta})\big)^\mathsf{T}\, \boldsymbol{\Sigma}_t^{-1}\, \boldsymbol{x}_t\,. \end{cases} \tag{4}$$

The two terms correspond respectively to the auto-correlation of the spectrally whitened point spread function (PSF) and to the data whitened spatially and spectrally and filtered by the shape of the whitened PSF. Remarkably, $A_{t,\boldsymbol{\gamma}_t}(\boldsymbol{\theta}_t(\boldsymbol{\mu}))$ and $B_{t,\boldsymbol{\gamma}_t}(\boldsymbol{\theta}_t(\boldsymbol{\mu}))$ provide sufficient statistics to study a potential source with orbital elements $\boldsymbol{\mu}$. An illustration of these terms is given in Fig. 1.

The maximum likelihood estimator of the spectrally integrated flux at epoch t with prior spectrum γ_t has an analytical expression that depends solely on the $A_{t,\boldsymbol{\gamma}_t}$ and $B_{t,\boldsymbol{\gamma}_t}$ terms:

$$\widehat{\alpha}^{\mathrm{int}}_{t,\boldsymbol{\gamma}_t}(\boldsymbol{\theta}_t(\boldsymbol{\mu})) = \underset{\alpha^{\mathrm{int}}_t}{\arg\max}\; \mathscr{L}_{t,\boldsymbol{\gamma}_t}(\alpha^{\mathrm{int}}_t, \boldsymbol{\theta}_t(\boldsymbol{\mu})) = \frac{B_{t,\boldsymbol{\gamma}_t}(\boldsymbol{\theta}_t(\boldsymbol{\mu}))}{A_{t,\boldsymbol{\gamma}_t}(\boldsymbol{\theta}_t(\boldsymbol{\mu}))}\,. \tag{5}$$

Given our model, $B_{t,\boldsymbol{\gamma}_t}(\boldsymbol{\theta})$ is Gaussian distributed of variance $\mathrm{Var}\{B_{t,\boldsymbol{\gamma}_t}(\boldsymbol{\theta})\} = A_{t,\boldsymbol{\gamma}_t}(\boldsymbol{\theta})$, which is supposed deterministic. The variance of the spectrally integrated flux estimate is in this case:

$$\mathrm{Var}\{\widehat{\alpha}^{\mathrm{int}}_{t,\boldsymbol{\gamma}_t}(\boldsymbol{\theta})\} = \frac{\mathrm{Var}\{B_{t,\boldsymbol{\gamma}_t}(\boldsymbol{\theta})\}}{A^2_{t,\boldsymbol{\gamma}_t}(\boldsymbol{\theta})} = \frac{1}{A_{t,\boldsymbol{\gamma}_t}(\boldsymbol{\theta})}\,. \tag{6}$$

As demonstrated in [12], the spectrally combined mono-epoch signal-to-noise ratio with prior spectrum $\boldsymbol{\gamma}_t$ follows a Gaussian distribution in the absence of source. At epoch t and position $\boldsymbol{\theta}$ the former given by:

$$\mathrm{S/N}_{t,\boldsymbol{\gamma}_t}(\boldsymbol{\theta}) = \frac{\mathbb{E}\{\widehat{\alpha}^{\mathrm{int}}_{t,\boldsymbol{\gamma}_t}\}}{\sqrt{\mathrm{Var}\{\widehat{\alpha}^{\mathrm{int}}_{t,\boldsymbol{\gamma}_t}\}}} = \frac{B_{t,\boldsymbol{\gamma}_t}(\boldsymbol{\theta})}{\sqrt{A_{t,\boldsymbol{\gamma}_t}(\boldsymbol{\theta})}}\,. \tag{7}$$

In addition, it was shown in [23] that explicitly accounting for the non-negativity of the exoplanet flux is beneficial and enhances the detection performance. In the following, we denote the positivity constraint by $\big[u\big]_+ = \max(0, u)$. For the estimator of the spectrally integrated flux under positivity constraint, it gives:

$$\widehat{\alpha}^{\mathrm{int}^+}_{t,\boldsymbol{\gamma}_t}(\boldsymbol{\theta}_t(\boldsymbol{\mu})) = \frac{\big[B_{t,\boldsymbol{\gamma}_t}(\boldsymbol{\theta}_t(\boldsymbol{\mu}))\big]_+}{A_{t,\boldsymbol{\gamma}_t}(\boldsymbol{\theta}_t(\boldsymbol{\mu}))}\,. \tag{8}$$

Finally, injecting the expression of $\widehat{\alpha}^{\mathrm{int}^+}_{t,\boldsymbol{\gamma}_t}$ in Eq. (3) enables to write the log-likelihood only as a function of the orbital elements $\boldsymbol{\mu}$:

$$\begin{aligned} \mathscr{L}_{\boldsymbol{\gamma}}(\boldsymbol{\mu}) &= c_2 + \frac{1}{2}\sum_t \frac{\big[B_{t,\boldsymbol{\gamma}_t}(\boldsymbol{\theta}_t(\boldsymbol{\mu}))\big]^2_+}{A_{t,\boldsymbol{\gamma}_t}(\boldsymbol{\theta}_t(\boldsymbol{\mu}))} \\ &= c_2 + \frac{1}{2}\sum_t \big[\mathrm{S/N}_{t,\boldsymbol{\gamma}}(\boldsymbol{\theta}(\boldsymbol{\mu}))\big]^2_+\,, \end{aligned} \tag{9}$$

whose maximum likelihood estimator under prior spectrum $\boldsymbol{\gamma}_t$ is:

$$\widehat{\boldsymbol{\mu}}_{\boldsymbol{\gamma}} = \underset{\boldsymbol{\mu}}{\arg\max} \left\{ \mathscr{C}_{\boldsymbol{\gamma}}(\boldsymbol{\mu}) = \sum_t \big[\mathrm{S/N}_{t,\boldsymbol{\gamma}}(\boldsymbol{\theta}(\boldsymbol{\mu}))\big]^2_+ \right\}. \tag{10}$$

This estimator has no closed-form expression and can only be approximated via global optimization numerical methods. The problem comes down to maximizing $\mathscr{C}_{\boldsymbol{\gamma}}(\boldsymbol{\mu})$ with respect to the orbital elements. This criterion combines optimally the information provided by the data and should increase the detection sensitivity, enable the detection of sources yet undetectable in individual epochs and simultaneously provide an estimation of their orbital elements.

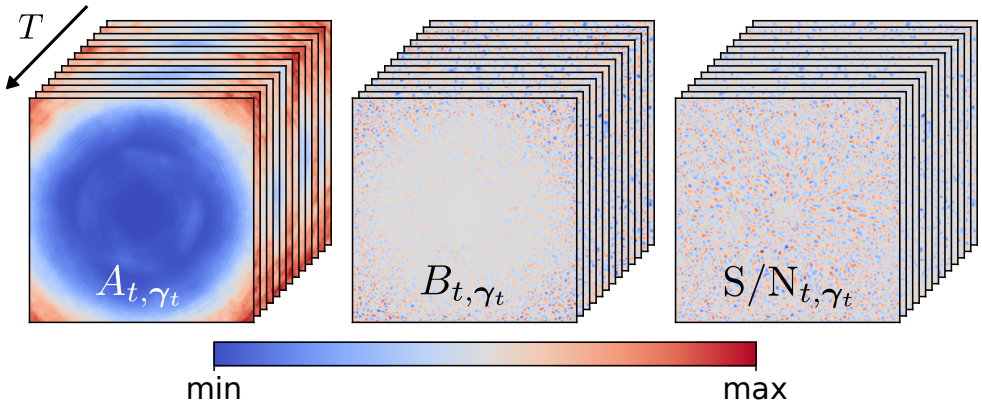

Figure 1: From left to right, mono-epoch A_{t,γ_t}, B_{t,γ_t} and $\mathrm{S/N}_{t,\gamma_t}$ maps computed with PACO.

2.3 Derivation of a multi-epoch signal-to-noise ratio

It is possible to use a matched filter approach [17, 18] and feed it with the previously derived maximum likelihood estimators. In this case, the best achievable multi-epoch S/N of any linear combination of the observed data, given a prior spectrum $\boldsymbol{\gamma} = \{\boldsymbol{\gamma}_t\}_{t=1:T}$, writes:

$$\mathrm{S/N}_{\boldsymbol{\gamma}}(\boldsymbol{\mu}) = \sqrt{\sum_t \left[\mathrm{S/N}_{t,\boldsymbol{\gamma}}(\boldsymbol{\theta}(\boldsymbol{\mu}))\right]_+^2} = \sqrt{\mathscr{C}_{\boldsymbol{\gamma}}(\boldsymbol{\mu})}\,. \tag{11}$$

It can be noted that this quantity is exactly the square root of the criterion $\mathscr{C}_{\boldsymbol{\gamma}}$ derived above. Hence, maximizing $\mathrm{S/N}_{\boldsymbol{\gamma}}(\boldsymbol{\mu})$ or $\mathscr{C}_{\boldsymbol{\gamma}}(\boldsymbol{\mu})$ with respect to $\boldsymbol{\mu}$ yields the exact same estimator for $\boldsymbol{\mu}$, as expected from the literature [17, 18]. Searching for the maximum likelihood estimator of $\boldsymbol{\mu}$ given our direct model is equivalent to searching for the orbital elements for which the best possible S/N is reached among all possible linear combinations of the reduced data collected along the apparent trajectory of the companion. The derived combination criterion is therefore optimal both in the maximum likelihood sense and in terms of S/N. For the rest of the paper, we refer to the multi-epoch $\mathrm{S/N}_{\boldsymbol{\gamma}}(\boldsymbol{\mu})$ of Eq. (11) when searching for the best estimator and assess the multi-epoch detection relevance.

We specifically developed the PACOME algorithm [5] to tackle the problem of finding a solution that maximizes Eq. (11). This algorithm aims at sampling the orbital elements parameter space, usually on a multi-dimensional grid. For each orbit sample, the method solves Kepler's equation to compute the associated 2-D positions projected on the detector at all given observation times, interpolates the A_{t,γ_t} and B_{t,γ_t} maps at these positions and computes the multi-epoch S/N. Once the search space has been sufficiently explored, the best orbital candidates, i.e. with the highest multi-epoch S/N, are optimized with a gradient-based numerical method, the best orbit of all is selected and finally its significance is assessed.

2.4 Multi-epoch noise distribution

As explained in Sect. 2.2, the mono-epoch spectrally combined S/N of Eq. (7) closely follows a normal distribution in the absence of source, which is very convenient to evaluate a potential detection as it is directly interpretable in terms of probability of detection and of probability of false alarm. On the other hand, the multi-epoch S/N derived in Eq. (11) is the square root of the sum of all squared non-negative mono-epoch S/N. To our knowledge such a distribution has no analytical form, making the detection evaluation more difficult. We thus compute the probability distribution function of the multi-epoch S/N distribution empirically by resorting to a Monte-Carlo approach. From this empirical distribution, we estimate the upper bound of the confidence interval associated to the confidence level $1-\rho \in [0,1]$ of a detection, with ρ a small number representing the targeted probability of false alarm. For that, we use the sample quantile function $\widehat{Q}_M(1-\rho)$ (threshold value below which random draws from the given distribution would fall $100\times(1-\rho)$ percent of the time) as defined in [16]. The probability density functions of the multi-epoch S/N in the absence of source computed by the Monte Carlo procedure are

shown in Fig. 2a and some values of the sample quantile function evaluated at different thresholds and for several degrees of freedom are given in Fig. 2b.

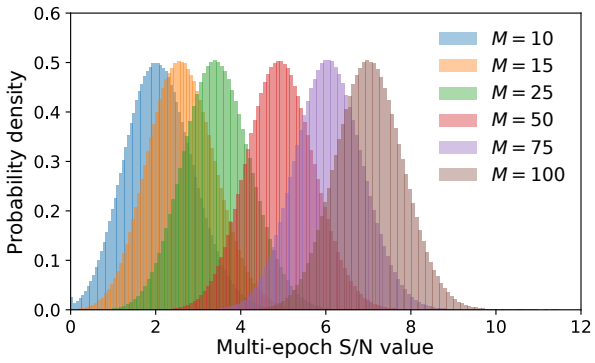

(a) Empirical multi-epoch S/N distribution for several dataset sizes M.

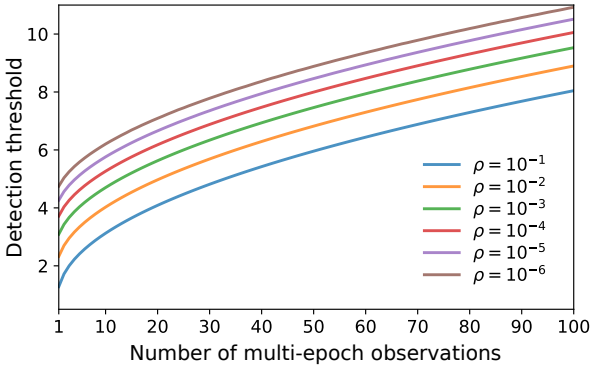

(b) Multi-epoch detection threshold estimated empirically for different confidence levels $1-\rho$.

Figure 2: Multi-epoch S/N distribution in the absence of source and associated detection thresholds.

3. APPLICATION ON REAL DATA: THE CASE OF HD 95086

3.1 Dataset description

We test the method on 13 datasets acquired with the InfraRed Dual Imaging Spectrograph (IRDIS) [9, 8] of the VLT/SPHERE instrument [1] and demonstrate the ability of the proposed algorithm to both detect faint sources and characterize their orbits. The observations are conducted with the ASDI technique using the pupil tracking mode of the instrument. The observations were scheduled so that the star was observed during meridian passage to take benefit, as best as possible, of the apparent rotation of the sought objects. All datasets correspond to observations of HD 95086 obtained in $K1$-$K2$ and $H2$-$H3$ spectral band under highly variable observing conditions spanning over 4.3 years between 2015 and 2019 cumulating a total exposure time of about 18 hours (see Table 1 for more information).

Table 1: Observing conditions of the considered ASDI sequences of HD 95086 acquired with the VLT/SPHERE-IRDIS. Columns are: ESO survey ID, observation date, spectral band (DB = Dual Band), number N_{frames} of temporal frames, total amount of rotation Δ_{par} of the field of view, individual exposure time DIT, total exposure time TDIT, coherence time τ_0, average seeing. Both coherence time and seeing estimations come from SPARTA or ESO's Astronomical Site Monitor when the former is not available.

ESO ID	Obs. date	Band	N_{frames}	Δ_{par} (°)	DIT (s)	TDIT (s)	τ_0 (ms)		Seeing (")	
							SPARTA	*ESO ASM*	*SPARTA*	*ESO ASM*
095.C-0298(H)	2015-02-03	DB K12	113	22.42	16	1808	-	22.95	-	0.665
095.C-0298(A)	2015-05-05	DB H23	64	22.44	64	4096	-	2.28	-	0.742
095.C-0298(A)	2015-05-05	DB K12	52	18.21	64	3328	-	2.14	-	0.774
095.C-0298(A)	2015-05-11	DB H23	64	22.48	64	4096	-	2.79	-	1.259
096.C-0241(G)	2016-01-18	DB K12	80	28.09	64	5120	32.98	-	0.444	-
097.C-0865(A)	2016-04-16	DB H23	80	28.14	64	5120	9.65	-	0.565	-
097.C-0865(B)	2016-05-30	DB K12	70	25.24	64	4480	2.44	-	0.599	-
198.C-0209(M)	2017-05-09	DB K12	100	36.6	64	6400	35.46	-	0.438	-
1100.C-0481(E)	2018-01-06	DB K12	70	41.01	96	6720	23.3	-	0.322	-
1100.C-0481(D)	2018-02-24	DB K12	64	33.45	96	6144	20.4	-	0.357	-
1100.C-0481(E)	2018-03-28	DB K12	64	33.29	96	6144	14.82	-	0.513	-
1100.C-0481(M)	2019-04-13	DB K12	63	33.8	96	6048	3.47	-	0.711	-
1100.C-0481(N)	2019-05-18	DB K12	64	33.23	96	6144	4.93	-	0.578	-

HD 95086 is a pre-main sequence A-type star of mass $M_\star = 1.6 \pm 0.1\, M_\odot$ [21] and parallax $\pi = 11.5659 \pm 0.0187$ mas [14]. Since 2013, the system is known to host HD 95086 b [21], a $4-5$ Jupiter mass exoplanet orbiting at a

separation of about $50-70$ au. This system has been widely studied, in particular to characterize the orbit of HD 95086 b, its atmospheric properties and to search for additional planets [21, 4, 7].

3.2 Reduction with PACO

Raw observations are pre-processed with the pre-reduction and handling pipeline of the SPHERE consortium [19]. Background, flat-field, bad pixels, registration, true-North, wavelength and astrometric calibrations are performed during this step. Additional custom steps implemented at the SPHERE Data Center [6] are also applied to refine the wavelength calibration, reduce the crosstalk, and improve the identification of bad pixels.

As all the datasets of this work were acquired in pupil-tracking mode (at a given epoch the field rotates around the star from a frame to another), knowing precisely the rotation center is critical to maximize the detection confidence and to derive accurate astro-photometric estimates of the putative sources in mono-epoch datasets. To ensure the good centering of our the datasets, we used the newly adopted routine of the SPHERE Data Center which has shown to improve the S/N of real sources [5].

After this pre-reduction step, raw observations are assembled in calibrated ASDI datasets. Each pre-reduced IRDIS observation is composed of $L=2$ spectral channels that are processed jointly. Calibrated ASDI datasets are processed with the PACO algorithm to produce, for each epoch, the $A_{t,\boldsymbol{\gamma}_t}$ and $B_{t,\boldsymbol{\gamma}_t}$ maps. These outputs serve as inputs of the PACOME algorithm. For simplicity, a flat prior spectrum (same weight for the two spectral channels) was chosen for each mono-epoch dataset reduced with PACO.

3.3 Re-detection of HD 95086 b

We carried a blind search with the PACOME method coded in Julia [2] on the 13 multi-epoch observations with a 7-D regularly space search grid sampled with 10 nodes per orbital elements totalling 10^7 explored orbits, see Fig. 2 for more details. We used a Catmull & Rom Spline for the sub-pixel interpolation (see [5] for details). To assess the relevance of any potential multi-epoch detection, we chose a confidence level of $\rho = 10^{-8}$ which corresponds to a multi-epoch detection threshold of $\widehat{Q}_{13}(1-10^{-8}) \simeq 7.2$. Evaluating the score of the 10^7 orbits and saving the ones above the chosen threshold typically took less than 2 min on a single thread of our local machine running at 2.40 GHz. All the 26×10^3 on-grid orbits yielding a combined signal higher than this threshold were then optimized locally to maximize their associated multi-epoch S/N via the VMLMB method [22].

Table 2: Search grid of the orbital elements explored by PACOME.

Not.	**Definition**	**Unit**	**Range**	$\boldsymbol{N}_{\text{nodes}}$
a	semi-major axis	mas	$46-1045$	10
e	eccentricity	-	$0-0.5$	10
i	inclination	deg	$0-180$	10
τ	epoch of periapsis passage	-	$0-1$	10
ω	argument of periapsis	deg	$0-360$	10
Ω	longitude of ascending node	deg	$0-360$	10
K	Kepler's constant	mas^3/yr^2	$2320-2631$	10

The optimal orbit found by PACOME yields a very significant detection of HD 95086 b with a multi-epoch S/N of 53.7 (compared to a multi-epoch detection threshold of 7.2). For comparison, the corresponding worst mono-epoch, mean mono-epoch and best mono-epoch S/N are 4.7, 14.0 and 21.3. Therefore, switching from mono-epoch to multi-epoch gives a average gain of 3.8 which is optimal as it scales with the square root of the number of epochs ($\sqrt{13}=3.6$). This optimal orbit, in the maximum likelihood sense, can be found in Table 3 and the corresponding mono-epoch and multi-epoch S/N maps centered on the solution are shown in Fig. 3.

3.4 Orbital elements characterization

Previous section showed that PACOME's grid search approach was able to re-detect HD 95086 b with a very high and unprecedented multi-epoch S/N. While the search grid method quickly gives a plausible orbital solution

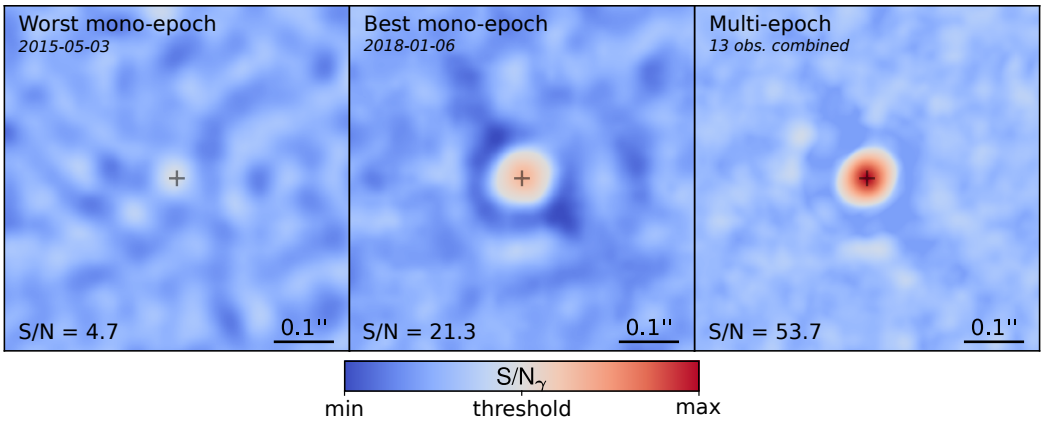

Figure 3: From left to right, worst mono-epoch, best mono-epoch and multi-epoch S/N maps around the optimal solution found by PACOME. The region of interest is sampled with 10 nodes per pixel. The colorbar is centered on the detection threshold (S/N = 5 for mono-epoch, S/N = 7.2 for multi-epoch).

whose projection on the detector passes through the point source at each epoch, it is not sufficient to represent accurately the statistical distribution of each orbital elements, which is often interesting information. Indeed, the orbital elements are known to be strongly degenerated thus more sophisticated approaches need to be considered to fully capture their non-symmetric, sometimes multi-modal, complex distributions. Several methods are often used in the literature to tackle this problem, most of which are based on Bayesian statistics, such as Markov Chain Monte Carlo (MCMC) or Nested Sampling (NS). Such methods tend to approximate (directly or indirectly) the posterior distribution of each parameter given a likelihood function and a prior probability distribution.

We chose the Nested Sampling algorithm and sampled from the posterior distribution of the orbital elements given the multi-epoch data using Julia's `NestedSamplers.jl` package of the `Turing.jl` ecosystem [15]. We used a cosine uniform distribution for the inclination i and uniform distributions for the other elements. We ran the algorithm with multiple ellipsoids to bound the prior space (similar to the MultiNest implementation [10]), 7000 active points, a rejection proposal (uniform sampling within the bounding volume) and the fraction of the remaining evidence `dlogz` ≤ 0.5 as stopping criterion. The median and 68% confidence intervals resulting from the posterior distribution are given in Table 3 and compared to the latest literature [7]. All the orbital elements we derive match those established by [7] within the errorbars except for t_0, the epoch of periapsis passage, which does not coincide to within 6.5 years. This difference corresponds to $1.4-1.9\%$ of the estimated period and could be explained by our slightly higher eccentricity e and smaller period P estimates. It is also worth noticing that the orbital characterization of [7] was performed with an MCMC method based on astrometric measurements (of the already detected source) and not blindly on direct imaging data directly as it is the case in this work, which is a much more complex and noisy problem. Corner plots of the orbital elements posterior distributions and the first thousand best (a posteriori) projected orbits are given in Fig. 4.

3.5 Multi-epoch contrast limit

With mono-epoch datasets, the achievable 5σ contrast is quantified for a given angular separation whereas, in a multi-epoch framework, the combined contrast is computed for a given orbit, where the angular separation of the source may vary along its trajectory. Hence, to compare the multi-epoch contrast to the more classical mono-epochs ones, we have to restrain the hypothesis and consider only face-on ($i = 0$) circular ($e = 0$) orbits. Given our model, we also need to assume that the flux of the source is constant over the epochs, which is consistent with face-on and circular orbits. These assumptions are restrictive but still more or less hold for the case of HD 95086. Under these hypothesis, the constant source flux equals:

$$\widehat{\alpha}^{\text{int}}_{t,\gamma_t}(\boldsymbol{\mu}) = \widehat{\alpha}^{\text{int}}_{\gamma}(\boldsymbol{\mu}) = \frac{\sum_t B_{t,\gamma_t}(\boldsymbol{\theta}_t(\boldsymbol{\mu}))}{\sum_t A_{t,\gamma_t}(\boldsymbol{\theta}_t(\boldsymbol{\mu}))}\,, \tag{12}$$

Table 3: Orbital elements of HD 95086 b found with PACOME. MLE represents the Maximum Likelihood Estimator of the orbital elements found in Sect. 3.3. NS represents the median and the 68% confidence intervals of the orbital elements marginal distributions estimated with the Nested Sampling algorithm described in Sect. 3.4. The results of this work are compared to [7] whose orbital elements a and K were converted using the quantities they used in their papers (star distance of 86.2 ± 0.3 pc, stellar mass $M_\star = 1.6 \pm 0.1$) and their period P was computed using Kepler's third law. For better comparability, our epoch of periapsis passage $\tau = t_0/P \pmod 1$ was re-expressed more conventionally as t_0 in years.

Elem.	**Unit**	**This work**		**Desgrange et al. 2022**
		MLE	NS	
$\boldsymbol{a}$	mas	1045.00	$732.17^{+73.31}_{-65.14}$	835^{+9}_{-242}
$\boldsymbol{e}$	-	0.23	$0.23^{+0.13}_{-0.08}$	≤ 0.18
$\boldsymbol{i}$	deg	139.19	$138.35^{+10.50}_{-23.37}$	144^{+18}_{-4}
$\boldsymbol{t_0}$	yr	1979.36	$1915.19^{+37.52}_{-88.68}$	2004^{+105}_{-45}
$\boldsymbol{\omega}$	deg	243.01	$274.58^{+28.22}_{-30.2}$ (+180)	271^{+110}_{-2}
$\boldsymbol{\Omega}$	deg	63.49	$100.31^{+26.24}_{-25.02}$ (+180)	72^{+53}_{-27}
$\boldsymbol{K}$	$\mathrm{mas}^3/\mathrm{yr}^2$	2631.00	$2479.67^{+49.45}_{-51.06}$	2498
$\boldsymbol{P}$	yr	658.59	$398.08^{+61.61}_{-52.50}$	483^{+8}_{-194}

and hence the associated multi-epoch contrast is given by:

$$\widehat{\sigma}_{\boldsymbol{\gamma}}(\boldsymbol{\mu}) = \sqrt{\mathrm{Var}\{\widehat{\alpha}_{\boldsymbol{\gamma}}(\boldsymbol{\mu})\}} = 1/\sqrt{\sum\nolimits_t A_{t,\boldsymbol{\gamma}_t}(\boldsymbol{\theta}_t(\boldsymbol{\mu}))}. \tag{13}$$

The mono-epoch and multi-epoch 5σ contrast curves computed with PACO and PACOME are shown in Fig. 5. Desgrange et al. [7] found a 5σ contrast of 2×10^{-6} at 0.6" with IRDIS for the best epoch (2018-01-06) whereas PACOME reaches an even deeper level with a multi-epoch 5σ contrast of 5.4×10^{-7} at the same separation. Again, the gain is 3.7, which is optimal as it scales as the square root of the number of epochs $\simeq \sqrt{13}\,(= 3.6)$.

3.6 Benefits of spectral whitened

We illustrate the importance of whitening the data spectrally in Fig. 6. The multi-epoch S/N maps of HD 95086 b with and without the spectral correlation corrections are compared. The source is intentionally masked to get a better idea of the residual noise in its vicinity. The colorbar is scaled and centered on the detection threshold at confidence level $\rho = 10^{-5}$ such that any signal above (in red) is considered a false alarm. When no spectral whitening is performed, a large number of structured patterns (noise and/or speckles) combine positively and increase the background signal, thus being above the prescribed detection level. Explicitly accounting for the spectral correlations reduces this side effect greatly so that solely the real known sources lie above the set detection limit. Indeed, the spectral whitening effect is undeniably efficient in reducing the number of false alarms, counted considering circular patches of the size of the FWMH, from 67 down to 0 at confidence level $\rho = 10^{-5}$. This effect is all the more pronounced the more spectral channels there are such, as with SPHERE-IFS, for example.

4. CONCLUSION

We developed a new source detection algorithm from multi-epoch ASDI observations based on a maximum likelihood and matched filter approach that combines optimally multi-epoch direct imaging datasets while accounting for the orbital motion of the sought sources. We also proposed a multi-epoch statistical framework to assess and control the confidence level of detection.

The method was applied to 13 datasets of HD 95086 observed with the SPHERE-IRDIS instrument, quickly re-detected the well-known planet HD 95086 b with an unprecedented S/N of 53.7 whose multi-epoch gain scales

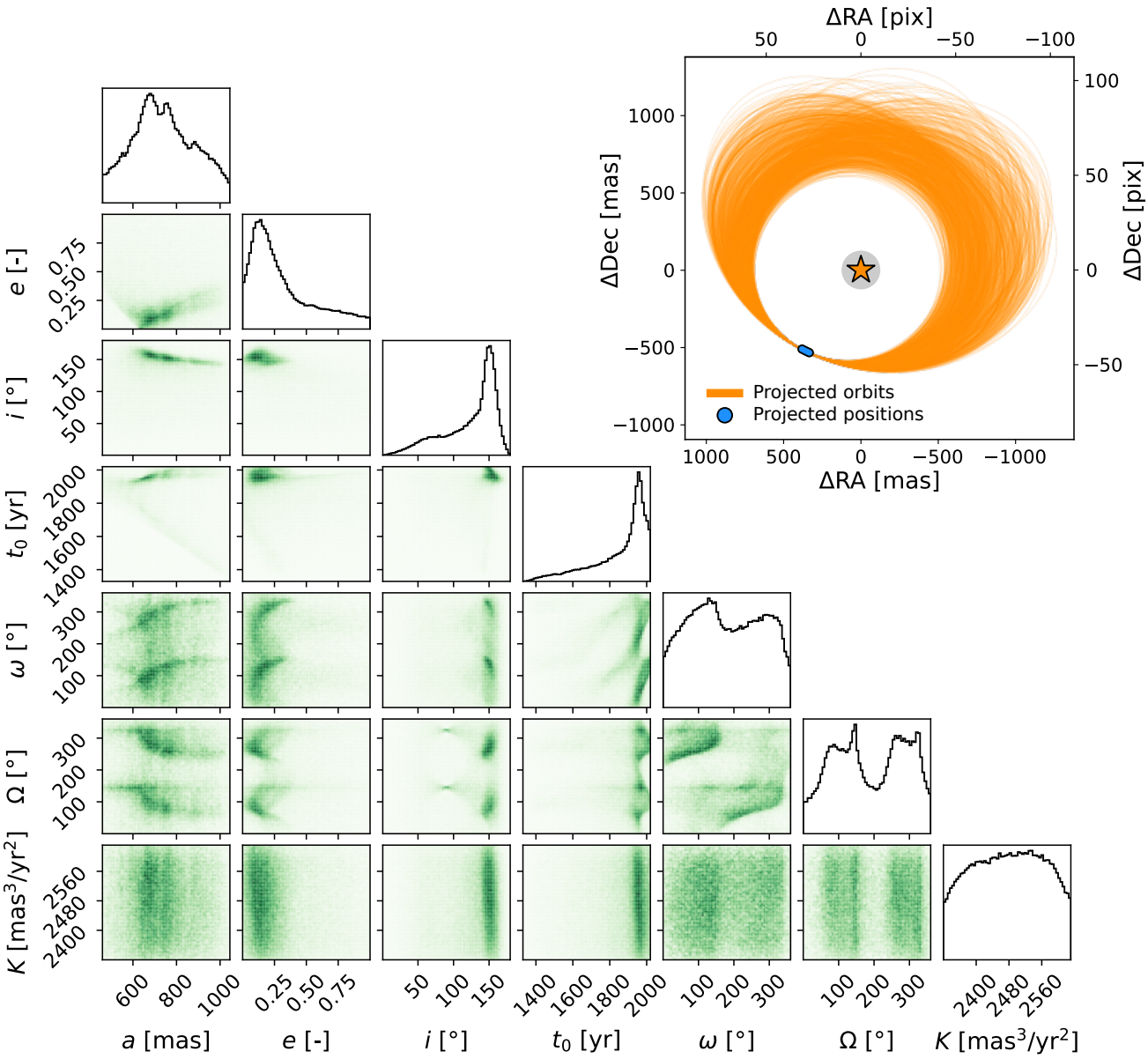

Figure 4: *Left)* Posterior distribution of each of the 7 orbital elements approximated with a Nested Sampling algorithm. *Upper right)* First thousand best (a posteriori) orbits projected on the detector. The blue dots represent the projected positions of HD 95086 b identified by PACOME.

with the square root of the number of epochs. We used a Nested Sampling algorithm to characterize its plausible ranges of orbital elements, all but one of which coincide with the latest literature. We reached with PACOME the deepest level of contrast to date with IRDIS, scoring a 5σ multi-epoch contrast of 1.9×10^{-6} at 0.2". Finally, we demonstrated the benefits of accounting for the strong spectral correlations of the ASDI data showing that doing so drastically reduces the number of multi-epoch false alarms.

In the future, the PACOME algorithm will be used on several other multi-epoch datasets to probe and search for currently hidden new exoplanet candidates. Other faster derivative-based sampling methods, such as Hamiltonian Monte Carlo, will be explored for the orbital characterization and other spatial covariance matrix estimation methods will be investigated, in addition to PACO, to improve the performances near the star. Finally, the

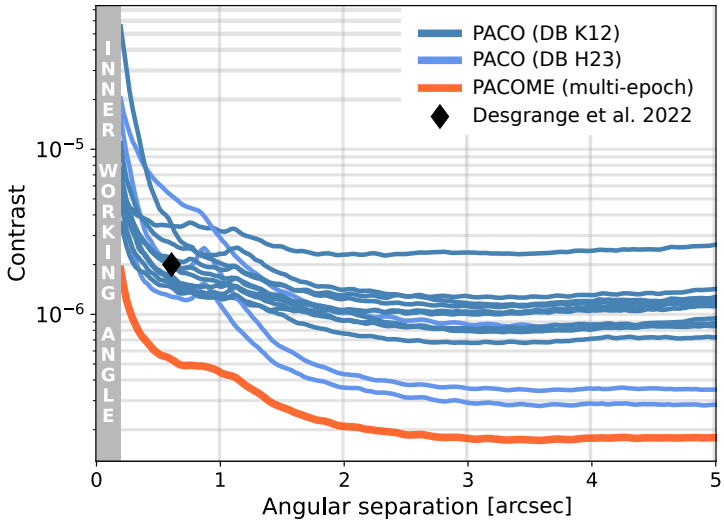

Figure 5: Mono-epoch contrast derived with PACO compared to the multi-epoch contrast obtained with PACOME for HD 95086 with IRDIS data assuming face-on circular orbits and a flux constant across epochs. The black diamond corresponds to the 5σ detection limit of Desgrange et al. 2022 [7] obtained for their best epoch with IRDIS.

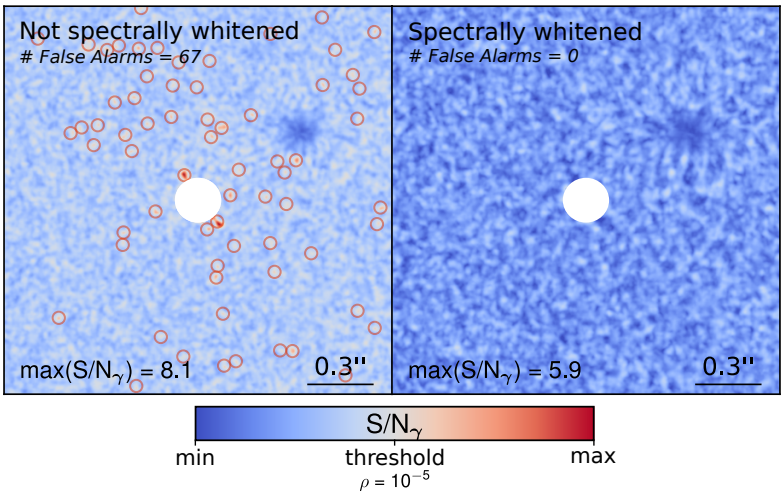

Figure 6: Comparison of the multi-epoch S/N maps for the not spectrally whitened and spectrally whitened data centered on the optimal orbital solution resampled with 10 nodes per pixels. The combined signal of HD 95096 b is masked and the color bar is centered on the multi-epoch detection threshold at confidence level $\rho = 10^{-5}$.

already available VLT/SPHERE-IFS multi-epoch observations will be reduced with PACO and the search for an additional planet in the inner region of HD 95086 will be carried out and presented in a future paper.

ACKNOWLEDGMENTS

This work has made use of the SPHERE Data Center, jointly operated by OSUG/IPAG (Grenoble, France), PYTHEAS/LAM/CESAM (Marseille, France), OCA/Lagrange (Nice, France), Observatoire de Paris/LESIA (Paris, France), and Observatoire de Lyon/CRAL (Lyon, France). This work has been supported by the French National Programs (PNP and PNPS), and by the Action Spécifique Haute Résolution Angulaire (ASHRA) of CNRS/INSU co-funded by CNES. This work used ESO archive data for HD 95086 from various observing programs whose ESO-IDs are listed in Table 1.

References

[1] J-L Beuzit et al. "SPHERE: the exoplanet imager for the Very Large Telescope". In: *Astronomy & Astrophysics* 631 (2019), A155.

[2] Jeff Bezanson et al. "Julia: A fresh approach to numerical computing". In: *SIAM review* 59.1 (2017), pp. 65–98. URL: https://doi.org/10.1137/141000671.

[3] F. Cantalloube et al. "Exoplanet imaging data challenge: benchmarking the various image processing methods for exoplanet detection". In: *Adaptive Optics Systems VII*. Ed. by Laura Schreiber, Dirk Schmidt, and Elise Vernet. Vol. 11448. Society of Photo-Optical Instrumentation Engineers (SPIE) Conference Series. Dec. 2020, 114485A, 114485A. DOI: 10.1117/12.2574803.

[4] G. Chauvin et al. "Investigating the young solar system analog HD 95086. A combined HARPS and SPHERE exploration". In: *Astronomy & Astrophysics* 617, A76 (Sept. 2018), A76. DOI: 10.1051/0004-6361/201732077.

[5] Dallant, J. et al. "PACOME: Optimal multi-epoch combination of direct imaging observations for joint exoplanet detection and orbit estimation". In: *Submitted to Astronomy & Astrophysics* (2023).

[6] Ph Delorme et al. "The SPHERE data center: a reference for high contrast imaging processing". In: *arXiv preprint arXiv:1712.06948* (2017).

[7] C Desgrange et al. "In-depth direct imaging and spectroscopic characterization of the young Solar System analog HD 95086". In: *Astronomy & Astrophysics* 664 (2022), A139.

[8] Kjetil Dohlen et al. "Prototyping of differential optics for the SPHERE IRDIS dual imaging planet finder camera". In: *SPIE Astronomical Telescopes + Instrumentation*. Vol. 7018. International Society for Optics and Photonics. 2008, p. 701859.

[9] Kjetil Dohlen et al. "The infra-red dual imaging and spectrograph for SPHERE: design and performance". In: *SPIE Astronomical Telescopes + Instrumentation*. International Society for Optics and Photonics. 2008, pp. 70143L–70143L.

[10] F. Feroz and M. P. Hobson. "Multimodal nested sampling: an efficient and robust alternative to Markov Chain Monte Carlo methods for astronomical data analyses". In: *Monthly Notices of the Royal Astronomical Society* 384.2 (Jan. 2008), pp. 449–463. ISSN: 0035-8711. DOI: 10.1111/j.1365-2966.2007.12353.x. eprint: https://academic.oup.com/mnras/article-pdf/384/2/449/3378518/mnras0384-0449.pdf. URL: https://doi.org/10.1111/j.1365-2966.2007.12353.x.

[11] Olivier Flasseur et al. "Exoplanet detection in angular differential imaging by statistical learning of the nonstationary patch covariances. The PACO algorithm". In: *Astronomy & Astrophysics* 618, A138 (Oct. 2018), A138. DOI: 10.1051/0004-6361/201832745.

[12] Olivier Flasseur et al. "PACO ASDI: an algorithm for exoplanet detection and characterization in direct imaging with integral field spectrographs". In: *Astronomy & Astrophysics* 637, A9 (May 2020), A9. DOI: 10.1051/0004-6361/201937239.

[13] Olivier Flasseur et al. "Robustness to bad frames in angular differential imaging: a local weighting approach". In: *Astronomy & Astrophysics* 634 (2020), A2.

[14] Gaia Collaboration et al. "Gaia Early Data Release 3 - Summary of the contents and survey properties". In: *A&A* 649 (2021), A1. DOI: 10.1051/0004-6361/202039657. URL: https://doi.org/10.1051/0004-6361/202039657.

[15] Hong Ge, Kai Xu, and Zoubin Ghahramani. "Turing: a language for flexible probabilistic inference". In: *International Conference on Artificial Intelligence and Statistics, AISTATS 2018, 9-11 April 2018, Playa Blanca, Lanzarote, Canary Islands, Spain*. 2018, pp. 1682–1690. URL: http://proceedings.mlr.press/v84/ge18b.html.

[16] Rob J. Hyndman and Yanan Fan. "Sample Quantiles in Statistical Packages". In: *The American Statistician* 50.4 (1996), pp. 361–365. ISSN: 00031305. URL: http://www.jstor.org/stable/2684934 (visited on 09/19/2022).

[17] Steven M Kay. *Fundamentals of statistical signal processing: Detection theory, vol. 2*. Prentice Hall Upper Saddle River, NJ, USA, 1998.

[18] Steven M Kay. *Fundamentals of statistical signal processing: Estimation theory, vol. 1*. Prentice Hall Upper Saddle River, NJ, USA, 1998.

[19] Alexey Pavlov et al. "SPHERE data reduction and handling system: overview, project status, and development". In: *Advanced Software and Control for Astronomy II*. Vol. 7019. International Society for Optics and Photonics. 2008, p. 701939.

[20] Laurent Pueyo. "Direct Imaging as a Detection Technique for Exoplanets". In: *Handbook of Exoplanets*. Ed. by Hans J. Deeg and Juan Antonio Belmonte. 2018, 10, p. 10. DOI: 10.1007/978-3-319-55333-7_10.

[21] J. Rameau et al. "Discovery of a Probable 4-5 Jupiter-mass Exoplanet to HD 95086 by Direct Imaging". In: *Astrophysical Journal, Letters* 772.2, L15 (Aug. 2013), p. L15. DOI: 10.1088/2041-8205/772/2/L15. arXiv: 1305.7428 [astro-ph.EP].

[22] Éric Thiébaut. "Optimization issues in blind deconvolution algorithms". In: *Astronomical Data Analysis II*. Ed. by Jean-Luc Starck and Fionn D. Murtagh. Vol. 4847. SPIE. Bellingham, Washington, 2002, pp. 174–183. DOI: 10.1117/12.461151.

[23] Eric Thiébaut and Laurent Mugnier. "Maximum a posteriori planet detection and characterization with a nulling interferometer". In: *Proceedings of the International Astronomical Union* 1.C200 (2005), pp. 547–552.